ORNL/TM-2021/2306
M3LW-22OR0402022

Experimental Evaluation of Deformation and Fracture Mechanisms in Highly Irradiated Austenitic Steels

M. N. Gussev
N. Bibhanshu
J. Dixon
T. M. Rosseel

October 2021

OAK RIDGE NATIONAL LABORATORY
MANAGED BY UT-BATTELLE FOR THE US DEPARTMENT OF ENERGY

ORNL/TM-2022/2306
M3LW-22OR0402022

Nuclear Energy and Fuel Cycle Division
Materials Science and Technology Division

Experimental Evaluation of Deformation and Fracture Mechanisms in Highly Irradiated Austenitic Steels

M. N. Gussev
N. Bibhanshu
J. Dixon
T. M. Rosseel

Date Published: October 2021

Prepared under the direction of the
U.S. Department of Energy
Office of Nuclear Energy
Light Water Reactor Sustainability Program
Materials Research Pathway

Prepared by
OAK RIDGE NATIONAL LABORATORY
Oak Ridge, TN 37831-6285
managed by
UT-BATTELLE, LLC
for the
U.S. DEPARTMENT OF ENERGY
under contract DE-AC05-00OR22725

This page intentionally left blank.

CONTENTS

This page intentionally left blank.

FIGURES

TABLES

ABBREVIATED TERMS

BORIS	BOR-60 Internal Study
BSE	backscattered electron
CEA	French Alternative Energies and Atomic Energy Commission
DOE	US Department of Energy
dpa	displacement per atom
EBR-II	Experimental Breeder Reactor II
EBSD	electron backscatter diffraction
EDF	Électricité de France S.A.
EDM	electrical discharge machine
EDS	energy-dispersive x-ray spectroscopy
GB	grain boundary
GND	geometrically necessary dislocation
GROD	grain reference orientation deviation
HR-EBSD	high resolution (or high angular resolution) electron backscatter diffraction
IASCC	irradiation-assisted stress-corrosion cracking
IPF	inverse pole figure
IQ	image quality
KAM	kernel average misorientation
LWR	light water reactor
LWRS	Light Water Reactor Sustainability program
NPP	nuclear power plant
ORNL	Oak Ridge National Laboratory
ROI	region of interest
SE	secondary electrons
SEM	scanning electron microscope/microscopy
YS	yield stress

This page intentionally left blank.

EXECUTIVE SUMMARY

The present report documents recent experimental results on the investigation of plastic deformation mechanisms and strain localization phenomena in austenitic steels irradiated by neutrons. Experiments were performed with specimens irradiated to 125 dpa and, additionally, with specimens that experienced radiation-induced swelling up to 3%.

Section 1 briefly analyzes the deformation localization in irradiated steels and its consequences on the material performance. The section describes the advantages and importance of the SEM-EBSD approach combined with in situ mechanical testing capability. Section 2 briefly introduces the experimental tools and methods (i.e., SEM/EBSD in situ tensile frame, electric discharge machine to manufacture irradiated specimens) and describes the investigated materials (element composition, irradiation conditions, and general microstructure).

Section 3 describes the key experimental results and provides a brief analysis and comparison with the datasets obtained earlier within the same task (i.e., low-dose specimens). The discussion focuses on EBSD microstructure maps with strain localization features, misorientation evolution as a function of strain, and observed deformation mechanisms. Section 4 evaluates data collected in recent years on highly irradiated steel and estimates the possible misorientation evolution under irradiation. The section introduces and discusses the concept of in-service-induced damage as an irradiation-assisted stress-corrosion cracking precursor.

Section 5 summarizes the work performed. As expected, the present work results are beneficial for exploring and understanding degradation mechanisms in highly irradiated in-core materials found in light water reactors after long-term in-service life.

This page intentionally left blank.

1. COMPLEXITY OF STRAIN LOCALIZATION PHENOMENON

It is now widely accepted that localized deformation is one of the driving forces of irradiation-assisted stress-corrosion cracking (IASCC) initiation. Neutron irradiation leads to switching in deformation modes from multiple fine slip lines to coarse dislocation channels and dislocation pileups at the grain boundaries (GBs) that may generate elevated local stresses [1–3]. The presence of areas with high local stresses and dislocation densities influences material performance and precedes stress corrosion crack initiation [3]. The negative role of dislocation pileups may be aggravated by second phases or strain-induced twinning inside the channel. The influence of dislocation channeling on corrosion is complex; in addition to elevated stresses and dislocation densities, channeling may lead to the oxide layer cracking.

Currently, there is still a limited understanding of localized deformation in irradiated austenitic steels—in-core materials of light water reactors (LWRs). A significant portion of the available literature focuses on the fine microstructure of the material and misses the grain level, as well as channel–GB interaction mechanisms. To perform analyses at an appropriate spatial scale, electron backscatter diffraction (EBSD) coupled with scanning electron microscopy (SEM) is employed as a powerful technique for studying the material structure and evaluating plastic deformation processes [1,4]. The SEM-EBSD approach [5–7] has excellent flexibility with regard to magnification and resolution level and allows for studying much larger areas compared to transmission electron microscopy. SEM-EBSD measures the crystal lattice gradients, quantifies strain-induced changes in the structure, and identifies deformation mechanisms, providing both spatial and crystallography information. This is especially important for evaluating nuclear power plant (NPP) components irradiated in-service and, especially, subjected to extended service life conditions.

However, very limited SEM-EBSD in situ data exist for NPP components, as well as for irradiated materials. As part of long-term efforts on LWR-relevant materials, the current project explores materials that have experienced radiation-induced damage with specimens hitting the 125 dpa mark.

This page intentionally left blank.

2. MATERIALS AND EXPERIMENTAL METHODS

2.1 SEM/EBSD IN SITU TESTING

SEM-EBSD in situ testing [5–7] is a key experimental approach in the present work. Specimens may be deformed in a step-by-step mode, keeping track of selected areas and features. Measurement may be performed under stress, which is important for high resolution (HR) EBSD (HR-EBSD, sometimes termed as High-Angular Resolution) and fracture analysis. During the testing, the specimen remains under vacuum, which preserves the surface quality and helps to avoid oxidation.

A TESCAN MIRA3 SEM, equipped with a high-speed Oxford Symmetry EBSD detector (resolution of 1244×1024 pixels in full-frame mode) and Oxford EDS detector was used. The EBSD indexing rate reached ~200 Hz in full-frame mode and ~3 kHz in 8×8 binning mode for freshly prepared specimens. Typical scanning rates during in situ tests with irradiated specimen were ~200–500 Hz (points per second) and varied slightly from specimen to specimen.

Miniature Kammrath & Weiss tensile frame with on-purpose designed grips and grips insertions [8] was installed in the SEM chamber, allowing for in situ mechanical testing. The frame supports both tensile and compression tests and includes an optional heater with a maximum temperature of 800°C.

2.2 INVESTIGATED MATERIALS

The present work included LWR-relevant materials (Table 1) irradiated in the Russian BOR-60 fast reactor in the framework of BORIS irradiation experiments and some later irradiation programs. The maximum damage dose reached 125 dpa.

Additionally, 304L steel irradiated in the Experimental Breeder Reactor (EBR-II) fast reactor [9] (Table 1) was included in the testing because of its reasonably high swelling level. Figure 1 shows the typical structure of the irradiated specimen using inverse pole figure (IPF), image quality (IQ), kernel average misorientation (KAM), and grain reference orientation deviation (GROD) maps. One may see annealed austenite structure with equiaxial grains; multiple annealing twins are present in the structure. Material may contain some retained ferrite, but the scans analyzed for the present work did not show any significant (i.e., a percent or more) ferrite amount. Table 1 lists the investigated materials and their irradiation conditions, and Table 2 provides element compositions.

Table 1. Materials and irradiation conditions.

Reactor	Material	Damage dose/irradiation temperature/swelling level	Purpose
BOR-60	304L	125.4 dpa, 320°C, negligible swelling	In situ testing to provide high-dose results
BOR-60	316L	~47 dpa, 320°C, no swelling data	Misorientation evolution under irradiation (see Section 4)
EBR-II	304L	~29 dpa, 430°C, ~3% swelling	In situ testing to provide high-dose results, misorientation evolution under irradiation

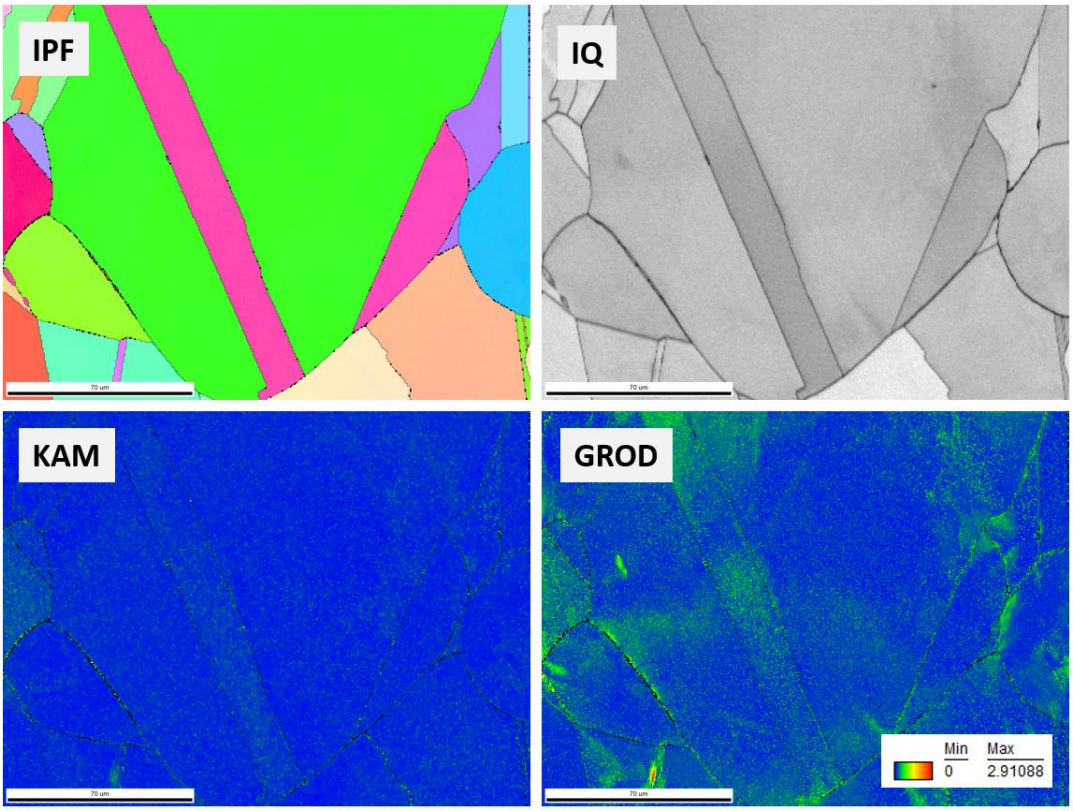

Figure 1. Microstructure of 304L steel irradiated in EBR-II fast reactor. 3E3A2B specimen; ID system corresponds to the one adopted in [9]. Phase map is omitted, as no significant amount of ferrite was observed. One may see mostly annealed austenite structure.

Figure 2 shows the radiation-induced void structure, imaged using the SEM/backscattered electron (BSE) technique described in [10,11]. This technique allows the evaluation of large areas and detects strain- and dislocation channeling–induced changes. While swelling is not usually anticipated under LWR-relevant conditions, it may occur at some locations in the core and maybe of concern at extended lifetimes. Therefore, it is important to evaluate the possible role of radiation-induced voids and deformation localization processes under these conditions in material with some degree of swelling.

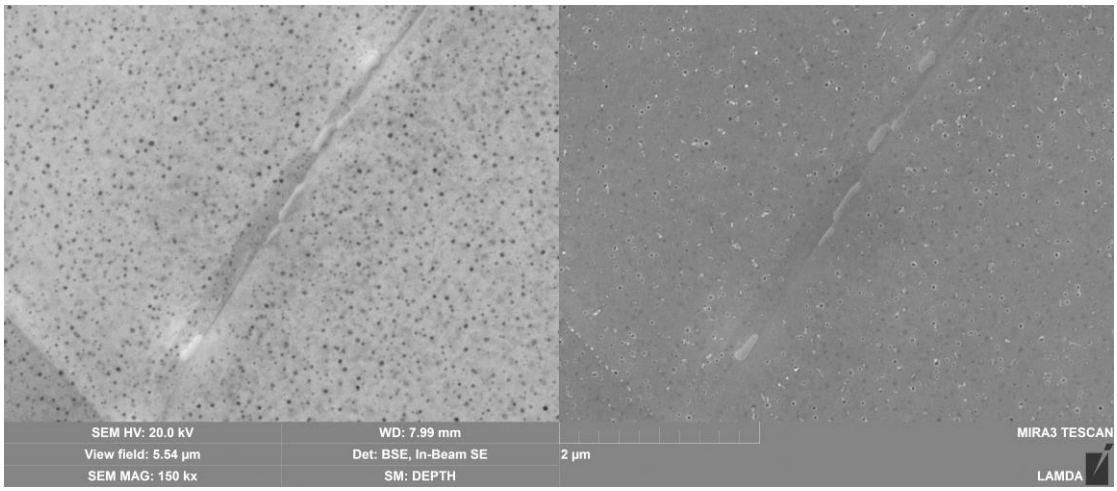

Figure 2. Swelling- and radiation-induced voids in the "Hex-block" material. (Left): BSE detector; (right): SEM detector. The image was recorded on the trial specimen (small debris piece) from 3E3A2B "Hex block" object (damage dose and swelling level are close to the 3E1C1B specimen, used for the current project). The surface was mechanically polished and electropolished; SEM analysis was performed within ~hours after preparation to keep the surface quality. Note the small working distance and high magnification level required for imaging the voids.

Table 2. Composition (wt. %) of the materials of interest

Material/ Reactor	Ref./ Secondary ID	Cr	Ni	Mn	Si	Cu	C	S	P	Mo	Co	N (ppm)	B (ppm)
304L/ BOR-60	304-1H [12]	18.61	9.88	1.79	0.36	0.25	0.022	0.0007	0.032	n/d	0.064	610	9
316L/ BOR-60	316-1E [12]	16.60	10.60	1.12	0.68	0.24	0.054	0.022	0.027	2.25	0.12	230	5
304L/ EBD-II	"Hex block" material [9]	19.26	8.81	1.57	0.43	n/d	0.056	0.03	0.027	n/d	n/d	n/d	n/d

n/d = no data

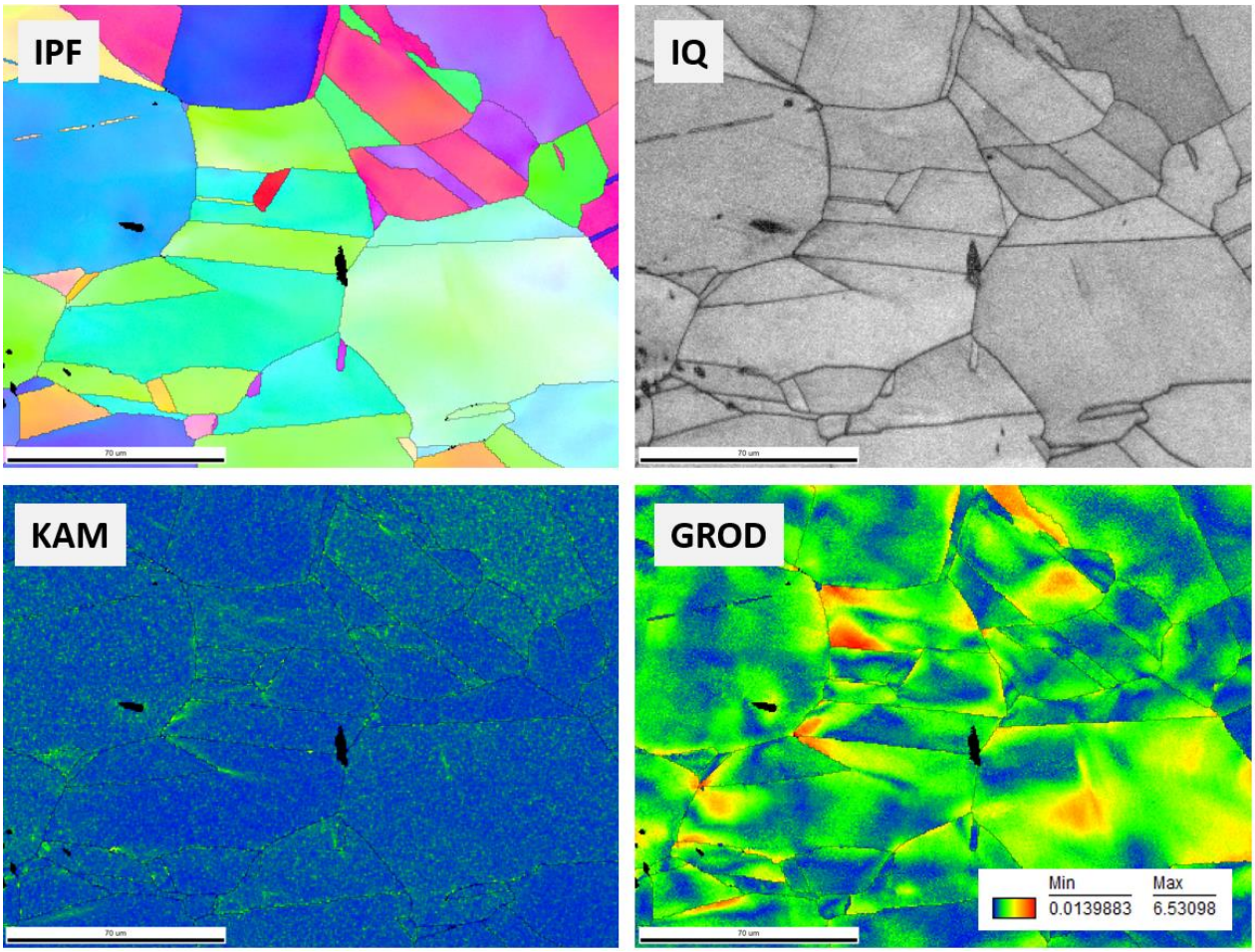

Figure 3. A typical microstructure of 304L steel, reference material for "Hex blocks" [9]. Phase map is omitted, as no significant amount of ferrite was observed. Note the signs of the cold work (lattice misorientation gradients) in the KAM and GROD maps.

2.2.1 The availability of archive materials

When analyzing radiation-induced changes in the material structures and properties, it is important to exclude possible artifacts. For instance, some second phases may be radiation-induced or present in the material before irradiation. Therefore, the availability of archive materials is an important advantage, strongly reducing the possibility of incorrect data interpretation. To perform the present work, authentic archive materials were available in a limited quantity for all steels listed in Table 2.

Reference BOR-60 304L and 316L steels were provided by Dr. B. Tanguy (Électricité de France S.A. [EDF] and French Alternative Energies and Atomic Energy Commission [CEA]). This reference material corresponds to the steel irradiated under EDF/CEA irradiation programs at the BOR-60 fast reactor.

Archived EBR-II 304L steel ("Hex blocks") was provided by Dr. F. A. Garner (Radiation Effects Consulting, Richland, WA). Figure 3 shows the microstructure of the 304L steel, the reference material for EBR-II-irradiated "Hex blocks" [9]. Analyzing the IPF map, one may see weak in-grain color

variations, reflecting lattice orientation gradients, as well as a fine needle-like twin present in one of the grains. In addition, the EBSD kernel average misorientation (KAM) map shows the increased KAM values near the GBs, and the grain reference orientation deviation (GROD) map reveals some bending of the grains. All these observations suggest some level of cold work, likely below 10%. This observation—some degree of cold work for the reference material vs. the mostly misorientation-free structure of irradiated steel—will be discussed in Section 4.

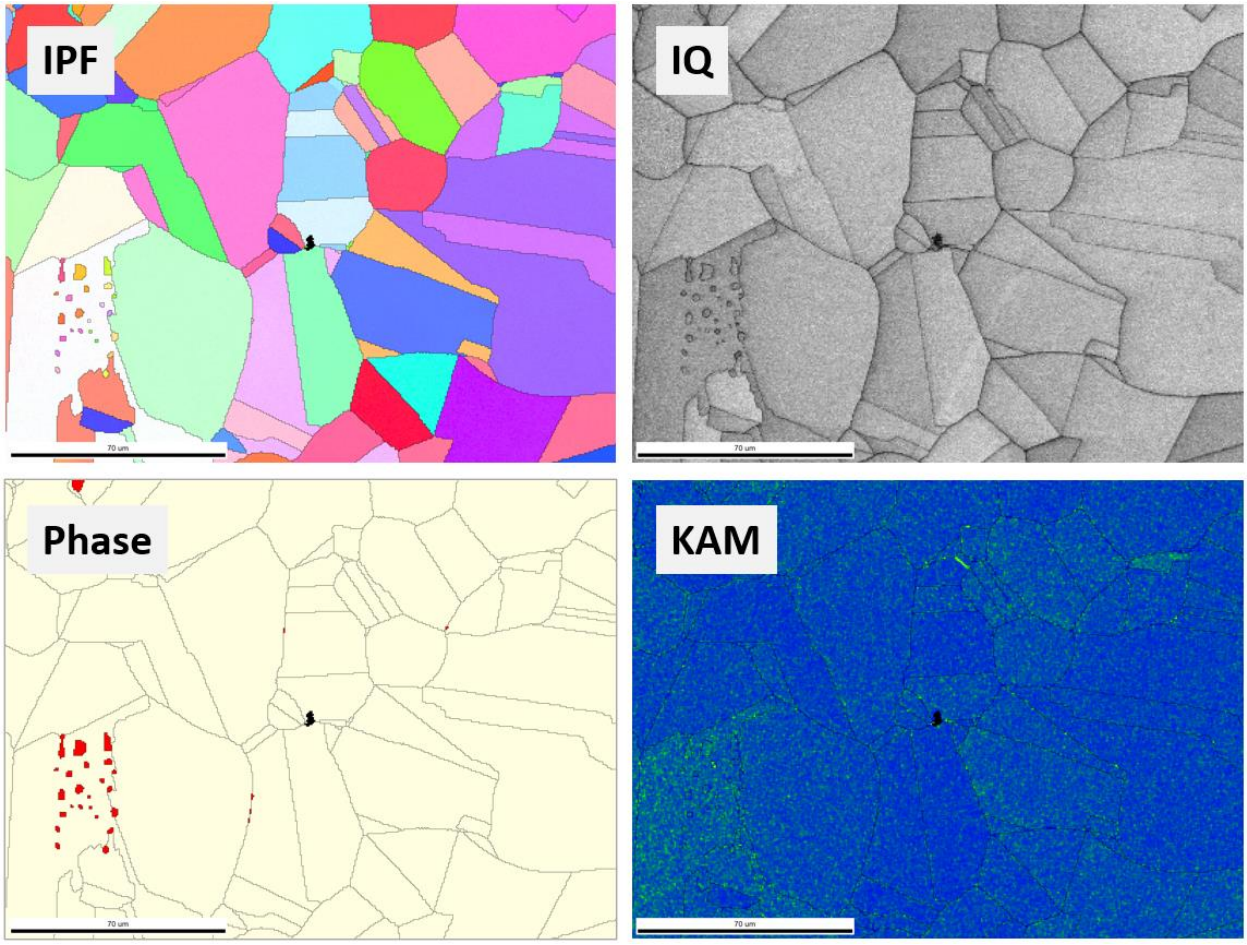

Figure 4. EBSD IPF, IQ map, phase map, and KAM map for the 125 dpa irradiated 304L steel studied in the present work. The material contains ~1 vol. % of retained ferrite, forming specific clusters or colonies in the structure (see an example in the left bottom corner of the Phase map). The IPF map is colored in the horizontal direction, which is the tensile direction during in situ mechanical tests.

Figure 4 shows the typical microstructure of the material included in the present work. One can see annealed austenite structure with fairly coarse austenitic grains of ~50–80 μm in size. The image quality (IQ) and KAM maps confirm the annealed material conditions; no signs of cold work are visible. Retained ferrite of ~1–1.5% presents as small grains, often forming specific clusters or chains.

2.3 SPECIMEN GEOMETRY, MANUFACTURING, AND PREPARATION

Miniature tensile specimens were manufactured using an electrical discharge machine (EDM) system installed in the Low Activation Materials Development and Analysis (LAMDA) facility hot area [8,13]. The AgieCharmilles CUT 200 Sp commercial system was purchased ~3 years ago with multiple wire diameters, providing an accuracy level of up to 5 µm. Cutting is performed on specimens fully submerged in water, reducing radiological risks and excluding any possibility of overheating. Travel distances in the x-, y- and z-directions are 350, 250, and 250 mm, respectively.

The available materials had a geometry of thin flat plates with dimensions of 5.5×3.5×1 mm (materials irradiated in BORIS) or ~12×10×0.7 mm (304L steel irradiated in the EBR-II reactor). Ultra-miniature specimens of SS-Teeny geometry (Figure 5) with a gauge length of 1.5 mm and width of 0.6 mm were employed [13]. The geometry provides a length-to-width ratio of 2.5 and at least 5 grains across the smallest dimension for typical austenitic steels with a grain size of 60–80 µm.

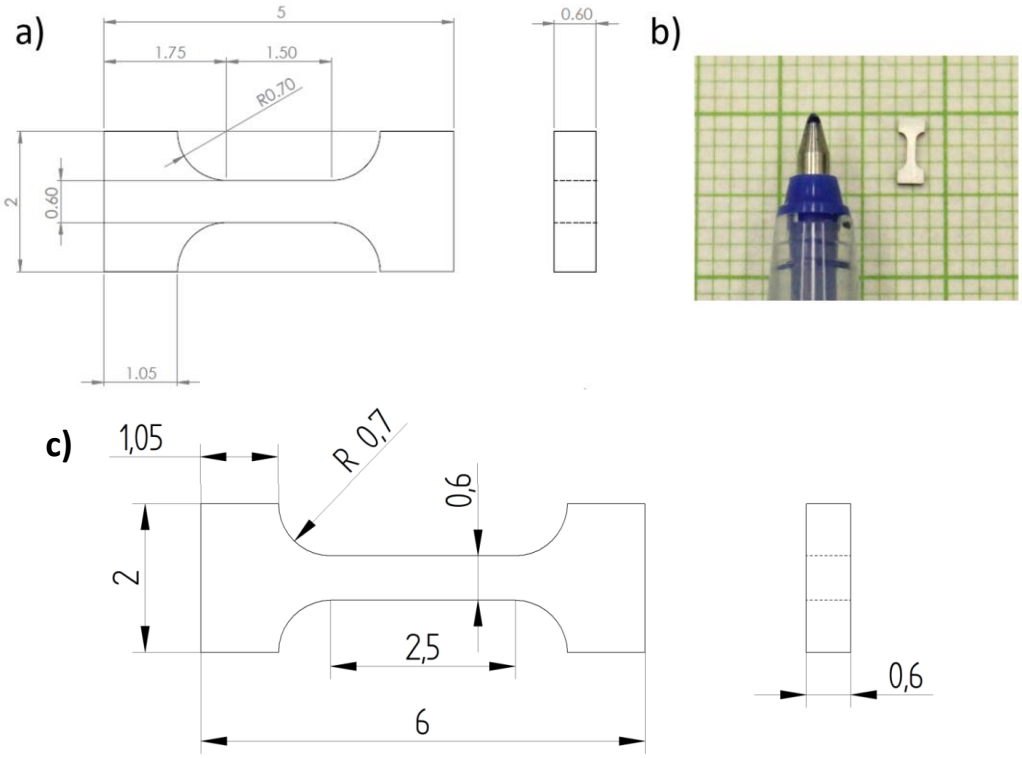

Figure 5. SS-Teeny specimen with 1.5 mm gauge (a, b [pen is used for scale]) and its version with elongated 2.5 mm gauge (c).

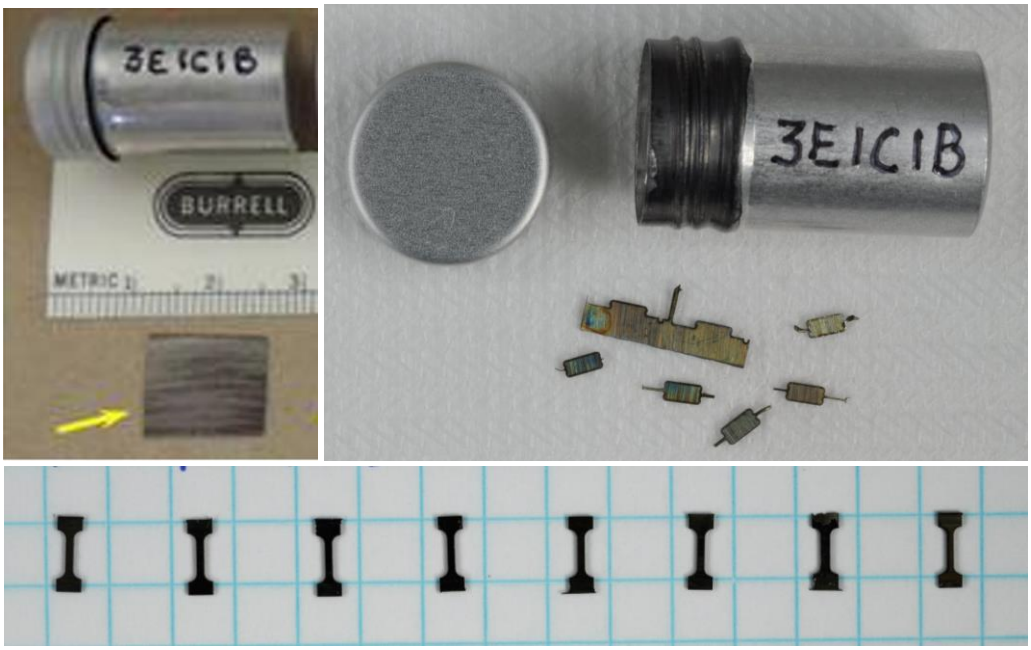

Figure 6. In-house manufactured tensile specimen. One may see images of the source irradiated plate of "Hex block material" (top left), remaining fragments (top right), and as-cut miniature tensile specimens with 2.5 mm gauge (bottom).

By analogy with previous work [8,13], electropolishing (Struer A2 solution, 30 V DC, ~5-sec duration) was selected as the final preparation step. Compared to colloidal silica polishing, this process excludes any contact with the surface being prepared and provides a clean metallic surface free of mechanical damage. As expected, the EBSD pattern quality is also better with the electropolished surface, compared to colloidal silica polishing. Electropolishing, however, requires careful solution selection, and the resulting surface may be slightly wavy compared to the colloidal silica polishing.

3. DEFORMATION MECHANISMS IN AUSTENITIC STEELS IRRADIATED TO HIGH-DAMAGE DOSES

3.1 TYPICAL IN SITU SEM/EBSD TEST

Based on the previous work [7,13], the 125 dpa specimen was deformed in the step-by-step mode (Figure 7). Tensile tests were conducted inside the SEM chamber that was coupled with the high-speed OXFORD EBSD detector (see Section 2.1). Selected regions of interest (ROIs) were analyzed at different stress and strain levels. Material behavior at stresses levels below yield stress (YS) (often termed as microplasticity) and at small plastic strains (below ~2–4%) was evaluated by conducting high-resolution EBSD (HR-EBSD) scans. HR-EBSD analysis requires recording of all Kikuchi patterns for the selected ROI at each step and posttest analysis to characterize the local changes in the geometrically necessary dislocation (GND) density and elastic stress fields [14,15]. To collect high-quality patterns, HR-EBSD data were collected at slow scan rates of 1–5 Hz. The HR-EBSD datasets are still being analyzed and will not be discussed in the present report.

Conventional EBSD data were recorded at each deformation step, once YS was reached. EBSD scans and SEM micrographs were recorded for each selected ROI to capture newly formed specific features of interest. Moreover, SEM and EBSD data were acquired for additional ROIs to document specific, often unique objects and structures (e.g., microcracks) that were formed under plastic deformation. Features and phenomena of interest include dislocation channel formation, strain-induced martensitic and deformation twin formation, and microfracture events.

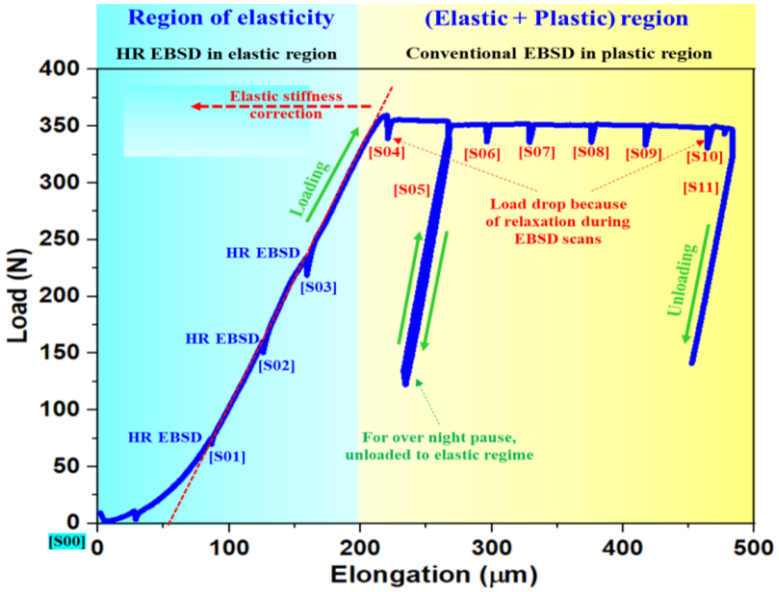

Figure 7. Load displacement diagram for the 125 dpa specimen. Zero step, [S00], provided reference datasets. HR-EBSD data was recorded from Steps [S01] to [S03]. SEM images were collected at each step to analyze dislocation channeling and microfracture processes. Full specimen ID: A32-2-1-TENSILE. The tests were completed in 2 days; the specimen was partially unloaded for night pause to minimize creep-associated processes.

The load-displacement curve recorded by the tensile frame software and associated deformation steps is presented in Figure 7. Figure 8 shows the general specimen view at different stages of deformation. Once the YS is exceeded and the specimen enters the elastic-plastic deformation mode, visible surface roughness appears at the middle of the gauge because of dislocation channel formation and evolution. As the experiment progressed, the plastically deformed area increased in size, covering approximately two-thirds of the total gauge length and forming a macroscopic neck. During the test, no pronounced cracking (i.e., cracks with a length of ~50–100 μm or larger) was observed. The experiment was stopped at ~450 μm total elongation, mostly because of strong Kikuchi pattern degradation.

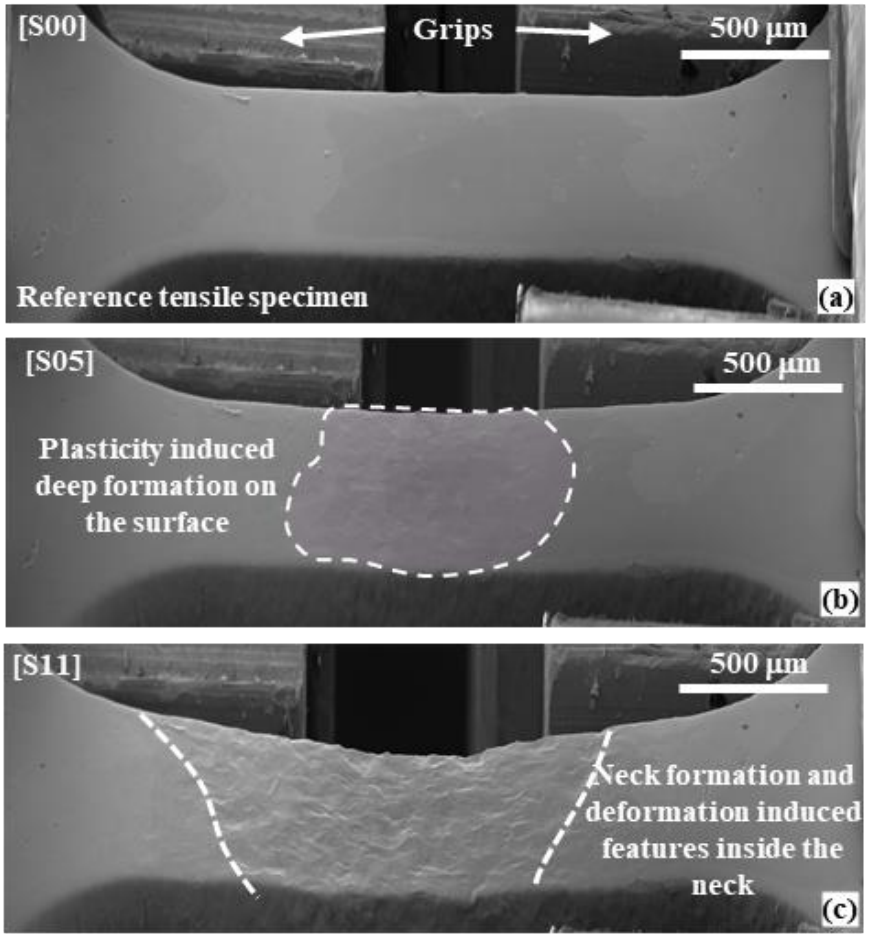

Figure 8. The gauge of the 125ndpa specimen at three different stages of the deformation. [S00]: reference image; [S05]: small plastic strains; [S11]: the final step of deformation (~20%, in engineering strain terms). All images were recorded at 70°-tilt and an SE detector.

Analysis of the developing neck revealed several microcracks below ~10–15μm (Figure 9). Additionally, specific features called “rough spots” were observed. Such “spots” had strong surface roughness because of the localized deformation and dislocation channeling. Also, some of the observed microcracks were found to form at such “rough spots.” As suspected, such surface features may form because of specific grain configurations (e.g., a combination of several “hard” grains with low Schmid factor), constraining local plastic deformation.

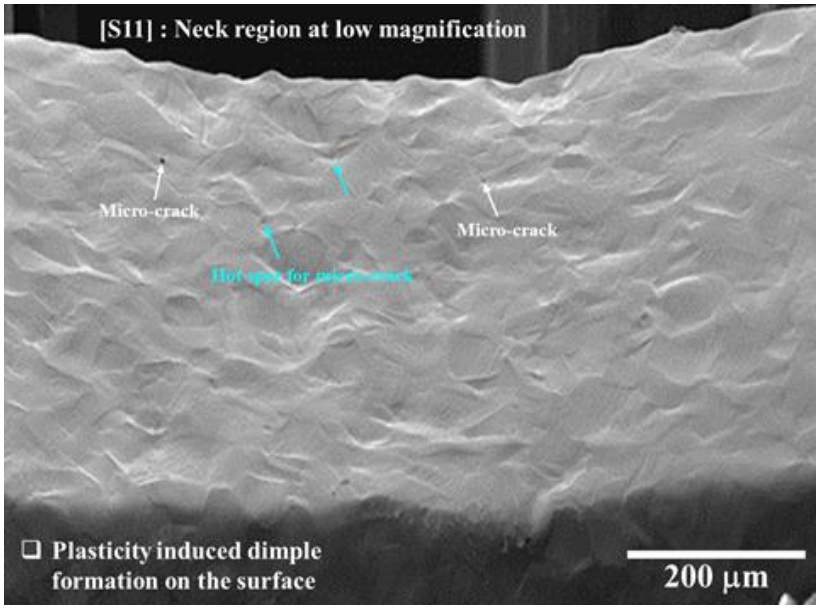

Figure 9. Microcracks in the neck of 125 dpa specimen. Full ID: A32-2-1-TENSILE. Arrows point to microcracks and specific "rough spots" with pronounced strain-induced roughness.

Figure 10 shows the SEM micrograph recorded at an elevated magnification at different steps of deformation. One may see pronounced changes in the surface morphology caused by plastic deformation and dislocation channeling. The appearance of the strain-induced features is very typical for irradiated austenitic steels, and no specific details related to high-damage-dose irradiation were observed.

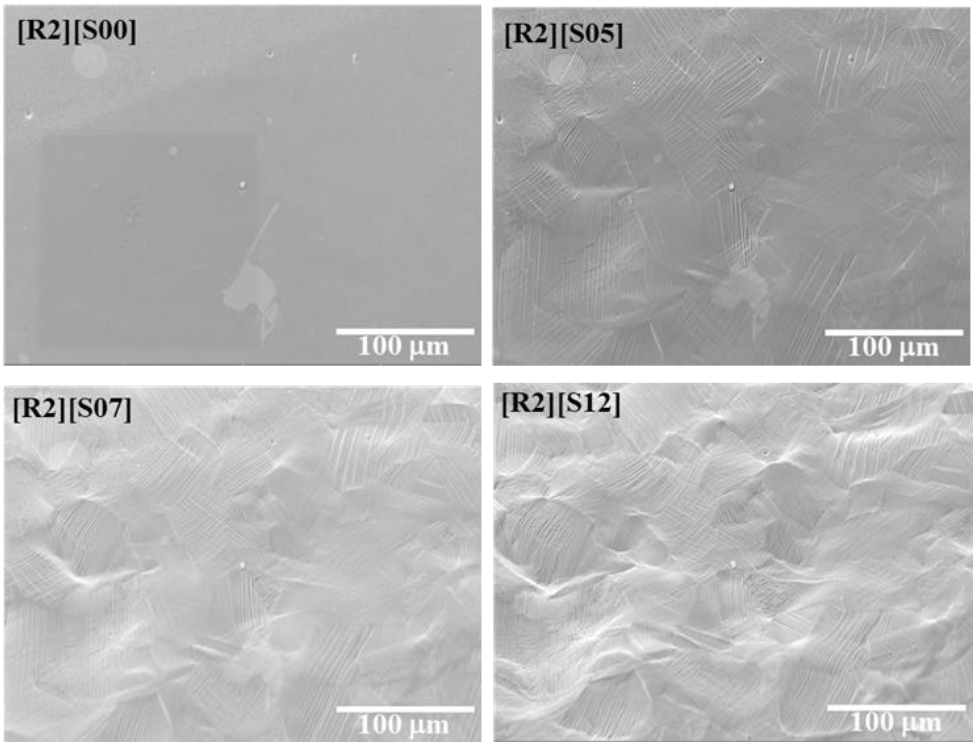

Figure 10. Surface morphology in 125 dpa specimen. Full ID: A32-2-1-TENSILE.

3.2 HIGH-DOSE BOR-60 MATERIAL

3.2.1 Mechanical Behavior of the Investigated Specimens

The load versus engineering strain for SS-Teeny miniature specimens, irradiated at different damage doses, are shown in Figure 11. The low-dose specimens were tested earlier, and the 125 dpa specimen, tested recently, represents the highest-damage dose assessed to date via in-situ testing. One may see that all tensile curves have a load drop soon after the YS point. The yield drop is followed by a short (~8–12% in the engineering strain terms) horizontal portion of the curve, resembling a "yield plateau." Following the plateau, the load continues to decrease, reflecting the formation of the neck. Additionally, all tensile curves contain "sharp" force drops, corresponding to the pauses in the deformation experiments to perform the SEM-EBSD data acquisition. No specimen was deformed until fracture due to the radiological limitations and safety rules.

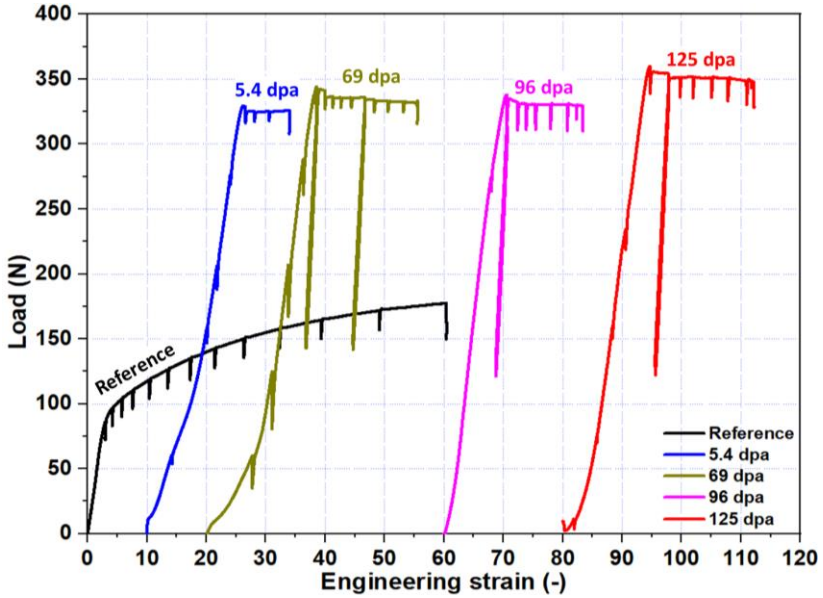

Figure 11. Raw tensile curves in the "load (N)-engineering strain" coordinates. The curves are shifted along the x-axis to aid the reader. Because the tests were interrupted before fracture, full elongation values for irradiated specimens and uniform elongation value for the reference specimen were not determined.

3.2.2 Microstructure Evolution in the 125 dpa Specimen

Figure 12 shows a typical EBSD dataset for a small plastic strain area for a 125 dpa irradiated specimen. The scanned area included at least ~40–50 grains of different sizes and orientations to provide sufficient statistics. Within the EBSD dataset, the IQ map represents the quality of the Kikuchi patterns; this qualitative parameter describes the visibility and contrast of the diffraction bands. Multiple approaches can be used to estimate the IQ value, and software vendors use different algorithms (often proprietary) to calculate IQ. However, in all cases, the lower IQ values (darker color) reflect poorer pattern quality and the presence of defects (at the surface or in the microstructure). The IQ value at a given location shows an obvious decrease once the dislocation channel forms. At Step [S06], the density of dislocation channels at some locations (dark-gray areas) is very high and makes EBSD data for these locations unreliable.

The inverse pole figure (IPF) maps show grain morphology and orientation; the color-coded lattice orientation representation is very convenient to highlight strain-induced changes. One may easily identify localized “hot spots” and lattice gradients, nucleating at the GBs and triple junction points once the specimen enters the elastic–plastic deformation mode. The GROD maps represent in-grain misorientation gradients [7]; being not very informative for nonirradiated austenitic steels, the GROD parameter clearly reveals the localized deformation areas (Figure 12, third row) in the irradiated and deformed specimen.

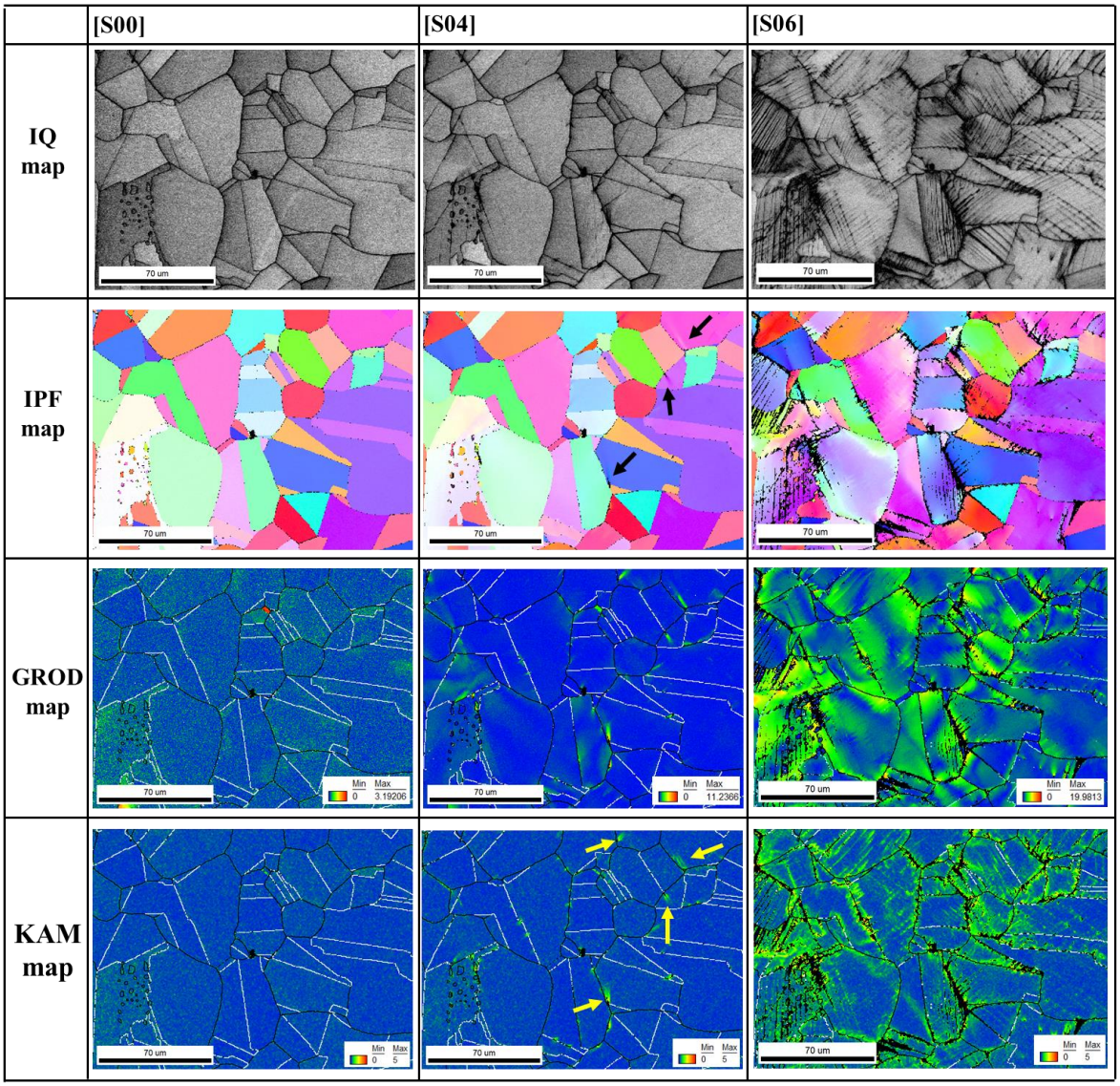

Figure 12. Typical EBSD dataset for small plastic strain area, 125 dpa specimen. The IPF maps are colored in the tensile direction (horizontal). Black arrows mark localized color changes in the IPF map, showing the misorientations introduced by the dislocation channel at Step 4; yellow arrows point to local “hot spots” in the KAM map.

Figure 13 shows additional IPF maps recorded at moderate strain levels for the same ROI. One may see a pronounced change in lattice orientation and the grain shape. Lattice rotation follows a general behavior

expected for metallic face-centered cubic (fcc) material: grains rotate toward the [001]–[111] line and, after that, toward [001] and [111] corners of the unit triangle, with respect to the tensile axis. Grains of "green color" (orientation close to ~[101]-corner of the unit triangle, with respect to the tensile axis) disappear from the structure as plastic strain increases. As an exception, in a large grain population, some grains or portions of grains may experience "abnormal" lattice evolution (see an example shown by the white circle in Figure 13).

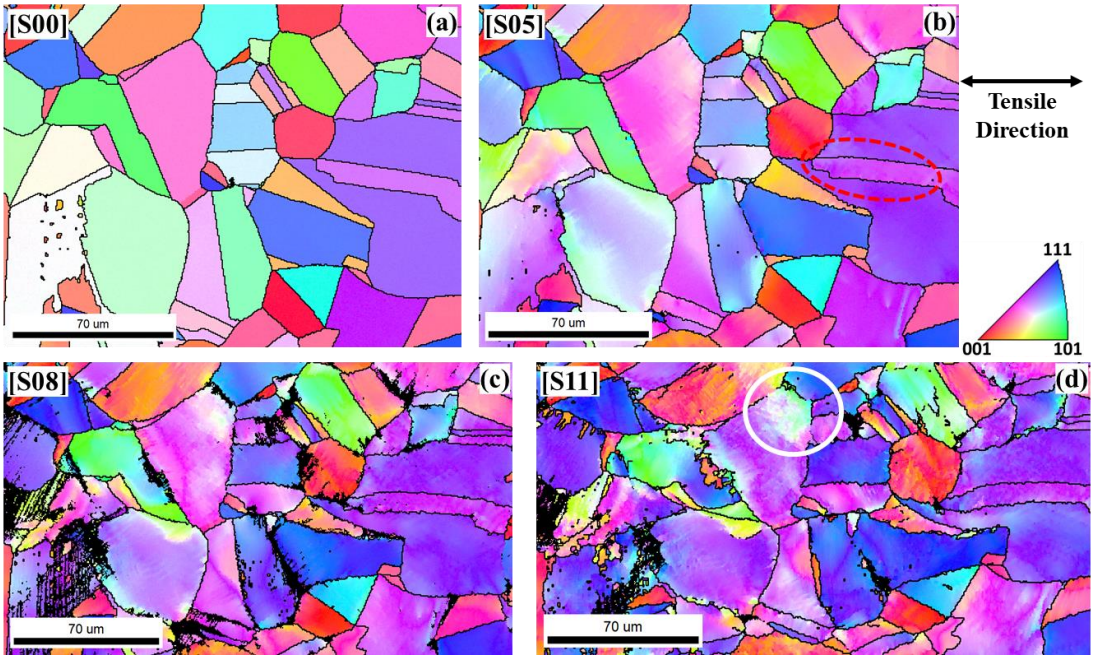

Figure 13. Microstructure evolution at moderate strain levels, 125 dpa specimen (A32-2-1-TENSILE). The color change is a sign of lattice gradient formation. Dashed red elliptical marked to represent the bending in the twinned grain.

Figure 14 shows the EBSD IPF map for the whole specimen gauge portion. The high performance of the Oxford Symmetry EBSD system allows for scanning the whole specimen gauge within a reasonable time (~ 1 h). It provides exceptionally large statistics on grain population, texture evolution, appearance and locations of "hot spots" (areas with highly localized strain), and plastic strain distribution within the neck. The detailed analysis will be given in a separate publication in combination with finite element modeling results.

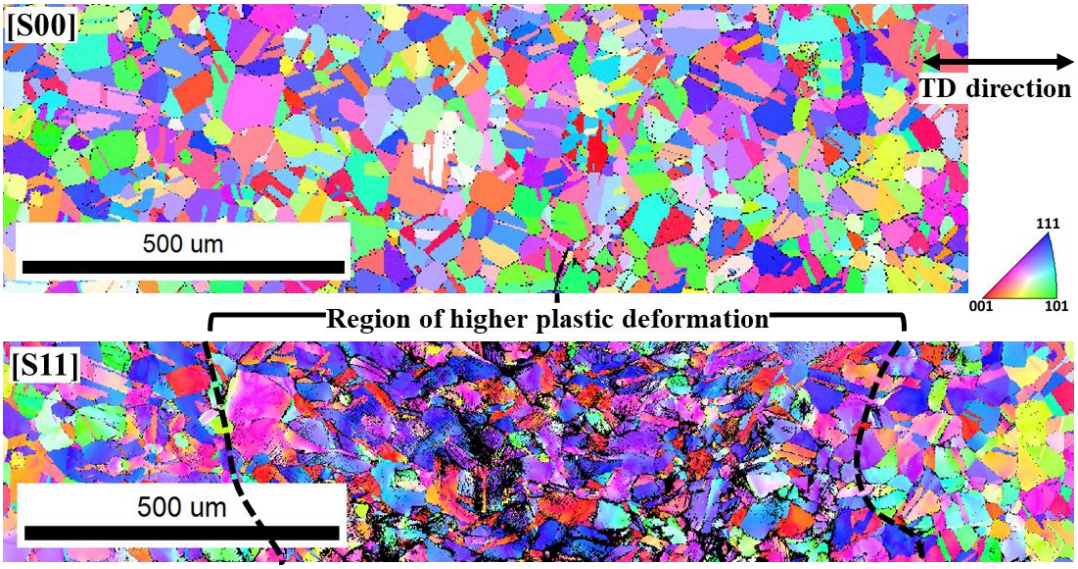

Figure 14. Low-magnification EBSD maps for the specimen gauge, 125 dpa specimen (A32-2-1-TENSILE).

3.2.3 Change in Crystallographic Texture with Deformation

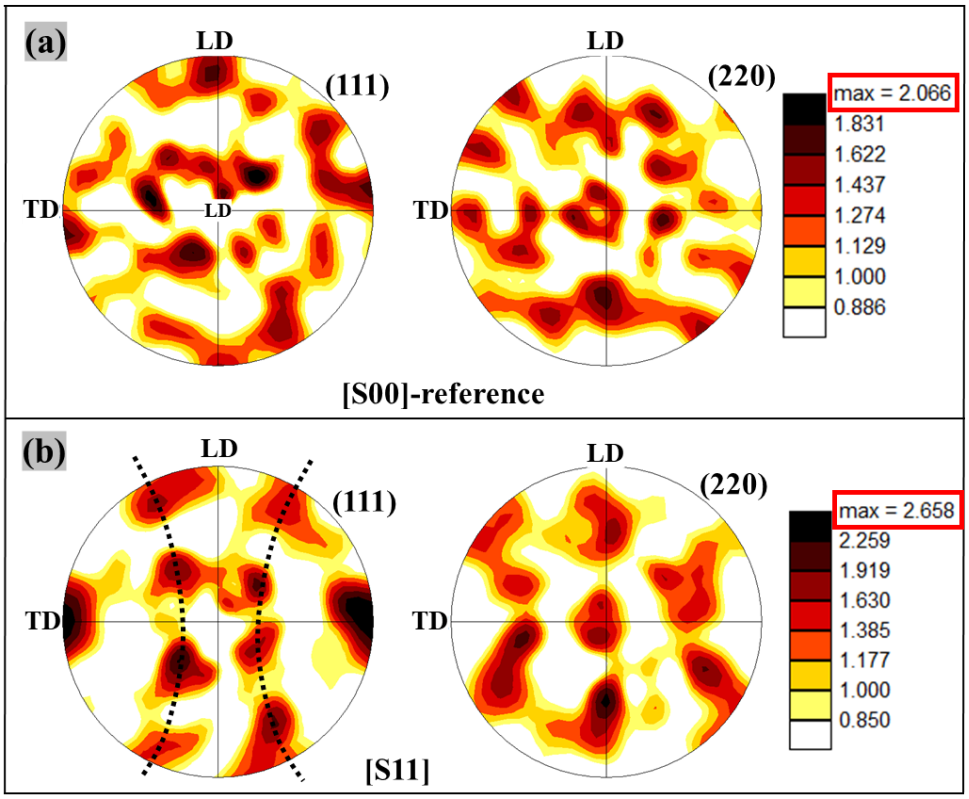

Figure 15. (111) and (220) pole figures, generated from the EBSD data for Steps [S00] and [S11] of deformation. TD: tensile direction.

Figure 15 shows the texture plots for the specimen gauge section at Steps [S00] and [S11]. Before straining (Step [S00]), the pole figures show weak texturing with a mostly random distribution of grain

orientations. At Step [S11], the specimen revealed well-visible texturing in the (111) and (220) pole figures and the signs of the transition towards the (001) ||TD and (111) ||TD fiber texture.

3.2.4 Microcrack Formation during In Situ Tensile Testing

Several minor microcracks, up to 10–15 μm long, were observed during the in situ test (see Figure 16 and Figure 17). In all cases, the crack initiation point was at the GB. No obvious connection of the cracks to ferrite grains, metallurgical inclusions, or preexisting defects were observed for the present specimen. Once formed, the cracks did not show a tendency to grow; the crack tips blunted, generating significant local plastic strain, visible as high local density of slip lines.

The crack formation mechanism is not clear, suggesting more work is necessary. Cracking may be connected to an inclusion directly below the surface; however, this is difficult to confirm without performing FIB (focused ion beam) milling. An alternate explanation may be the presence of some constraints to the plastic strain (e.g., local grain configuration makes plastic deformation more difficult, leading to rotation or strain incompatibility and microcracking).

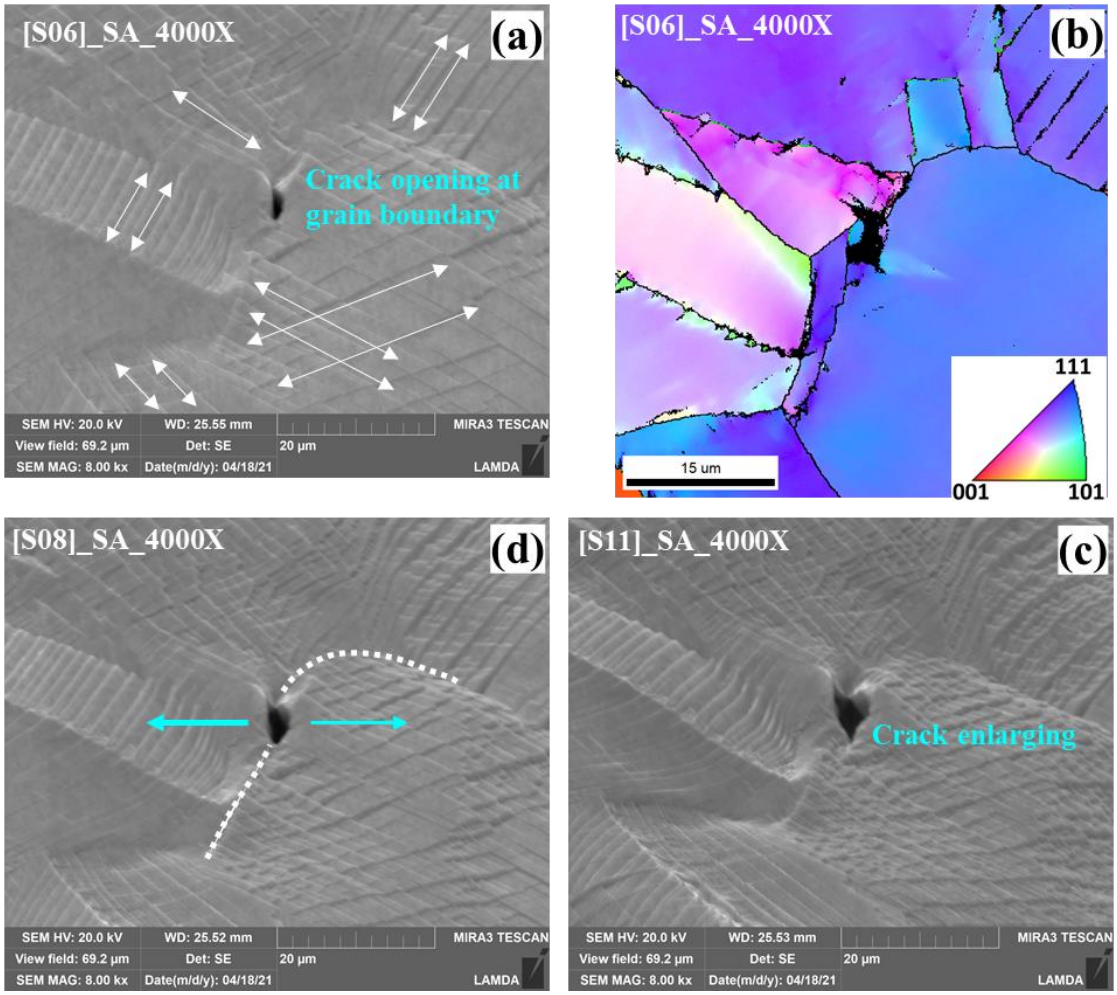

Figure 16. Evolution of microcrack associated with plastic strain increase at a GB. The final crack size was ~8–12 μm, 125 dpa irradiated specimen (A32-2-1-TENSILE). Note the specimen surface is 70°-tilted.

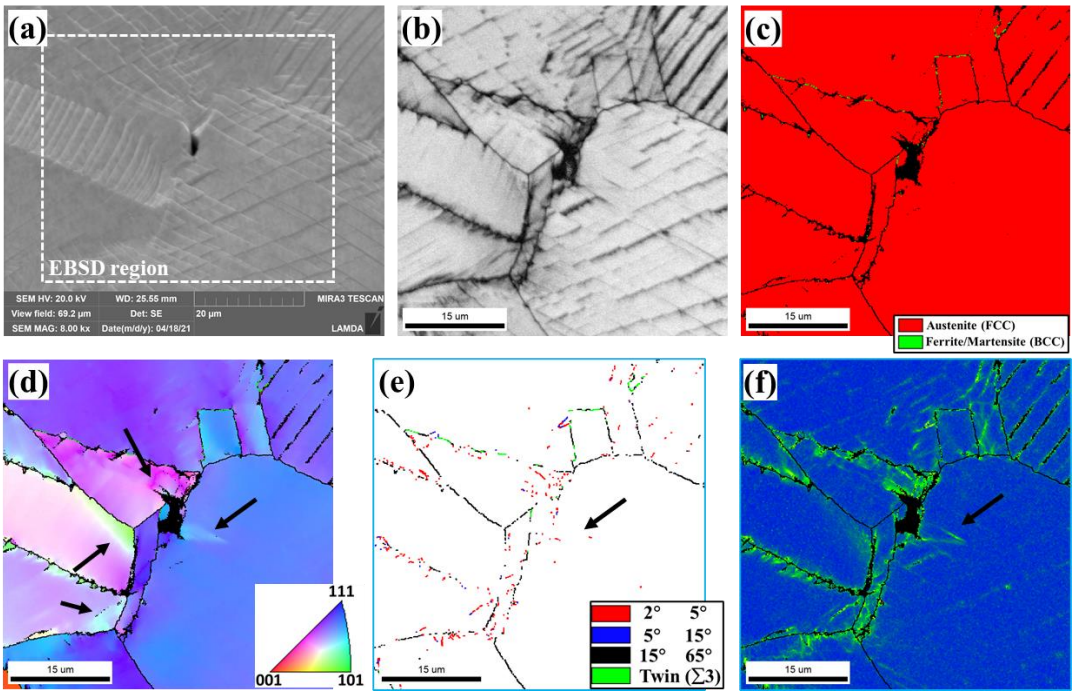

Figure 17. EBSD dataset for the area near the crack. (a) SEM image, (b) IQ map, (c) Phase map showing pure austenite structure, (d) TD (tensile direction colored) IPF map revealing dominating grains with ~[111] orientation with respect to the tensile axis (such grains have low Schmid factor values), (e) GB map, also showing multiple in-grain boundaries (2–5°) likely of dislocation nature, and (f) KAM map depicting the localized misorientation change along the crack. EBSD scan ID: [S06] _SA_4000X.

Further data analysis is in progress to compare the high-dose (69–125 dpa) and low-dose (~5 dpa) specimens and reference material.

4. MICROSTRUCTURE EVOLUTION UNDER IRRADIATION

As discussed in the introduction, localized deformation is an important (or even mandatory) condition for IASCC initiation [3]. Although the exact crack initiation mechanism is not clear, one may expect that, once dislocation pileup is formed at the GB, crack initiation becomes a likely event due to the combination of high local stresses, elevated local density, and external stress.

Formation of areas with increased dislocation density (i.e., "hot spots," dislocation pileups) during occasional loading reflects the concept of "service-induced damage" [16,17]; this concept is often used for cases of fatigue or creep damage (most often, microcracks and discontinuities in the structure). Potentially this concept may be extended to in-reactor components. If one adopts this concept, the likelihood of IASCC initiation may be assessed not only via the nominal damage dose value, but also via analyzing the localized strain areas (i.e., service-induced damage).

Assuming that the external stress was sufficiently high to stimulate plastic deformation but did not last long enough to cause crack initiation, it allows one to question what will happen to the localized deformation "spot" if the stress is removed. May one expect a disappearance of the "hot spot" (i.e., dislocation pileup) with damage dose increase, if irradiation continues? If yes, how fast?

A more general question may be whether EBSD is a suitable tool to detect the radiation-induced changes in the structure. The available database may provide at least a preliminary answer.

4.1 IRRADIATION AT 320°C

Figure 18 shows the microstructure of the cold-worked 316L steel before and after ~47 dpa irradiation. Clear signs of cold work—in-grain lattice gradients, grain bending, multiple fine twins of needle-like shape—are visible in both cases. High-dose irradiation (i.e., ~47 dpa at LWR-relevant conditions) did not lead to the disappearance of the signs of cold work signs or visible changes in the misorientation level. Additionally, no EBSD-resolvable grains or particles of radiation-induced second phases (e.g., ferrite) were detected.

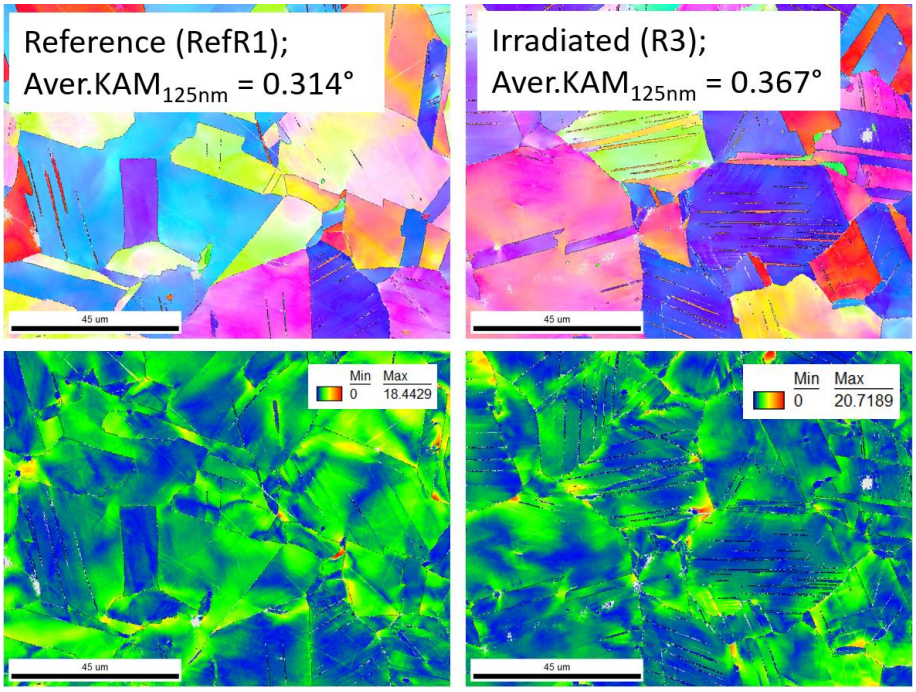

Figure 18. EBSD IPF and GROD maps for the reference and high-dose irradiated (~47 dpa) 316L steel. The insets show the average KAM values for the given maps. Note the 125 nm EBSD step (pitch) size.

Quantification of radiation-induced changes via KAM value (see insets in Figure 18 and Figure 19) show a very weak tendency toward KAM increase under irradiation. However, the KAM increase amplitude (less than 0.1°) appears to be small and may be attributed to the natural variations between the specimens or some difference in specimen preparation). It is important to underline that EBSD-related strain metrics, like KAM, are sensitive to the GNDs only. Stochastically stored dislocations are difficult to quantify via EBSD.

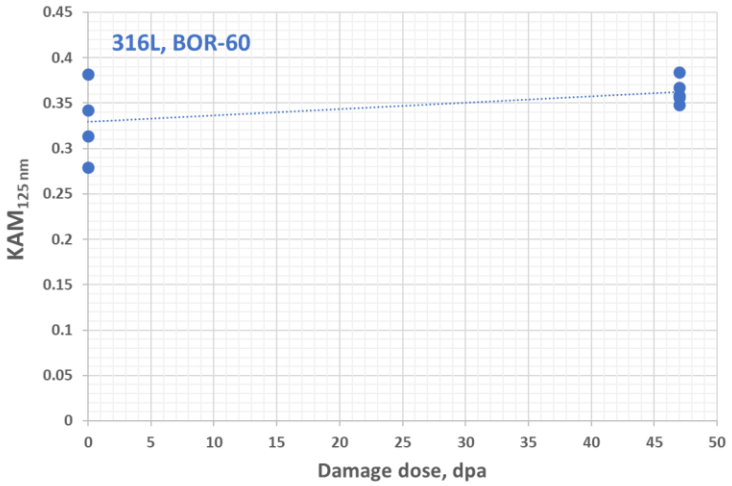

Figure 19. KAM versus damage dose for 316L steel irradiated in BOR-60 fast reactor. All data points are shown (no averaging) to illustrate scattering. Note the different EBSD steps in this figure compared to Figure 20 (125 nm and 0.5 µm, respectively).

Figure 19 shows all available data points (from EBSD scans) for the reference (0 dpa) material (cold-worked round bar). These EBSD scans, performed at the same time, using the same SEM settings, were randomly distributed along the specimen with dimensions ~12 × 4 mm. The difference in KAM was ~0.10–0.12°. As a very rough analogy, 0.1° misorientation corresponds to ~2% plastic strain for nonirradiated steel.

The EBSD data for the irradiated specimen were collected over the area with dimensions ~5 × 3.5 mm (i.e., much smaller, compared to the reference), and the maximum difference did not exceed ~0.05°. Although the average values suggest a minor increase in KAM under irradiation, the scattering of data points does not support this observation. Being conservative, one must conclude that the KAM value experiences no visible changes in cold-worked 316L steel during irradiation under given conditions (i.e., 320°C).

Figure 20 shows the KAM values for annealed 304L steel irradiated in the BOR-60 fast reactor at different damage doses. The difference between the reference specimen and specimens irradiated at 5–125 dpa is relatively weak, about 0.10–0.15°. No visible changes in the EBSD maps (not shown in the present report) were observed. Therefore, one may conclude that the KAM evolution during irradiation at 320°C is also weak, reflecting very minor, if any, changes in the GND density and distribution.

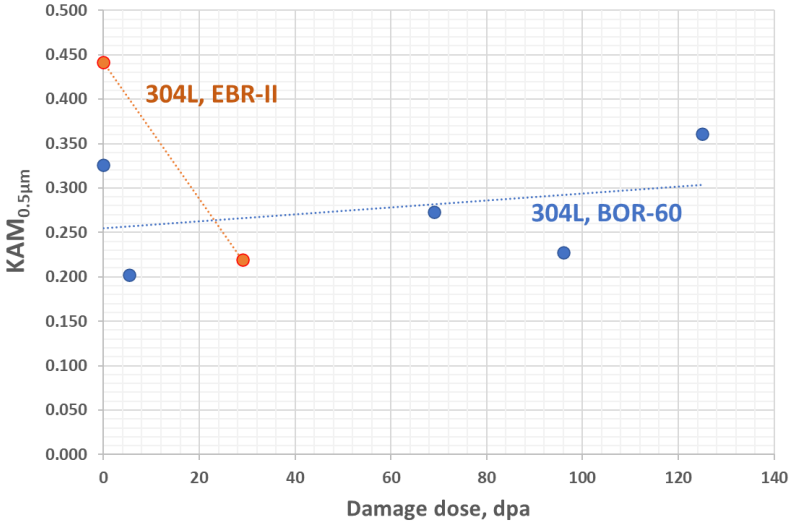

Figure 20. KAM value changes as a function of the damage dose for 304L steel. Note the different irradiation conditions (temperature) for EBR-II and BOR-60 reactors (see Section 2.2 and Table 1). Each data point represents an average value for 2–5 scans made under identical conditions.

4.2 IRRADIATION AT 430°C

Figure 21 shows the "Hex block" material (see Section 2) before and after irradiation. One may see clear changes in the structure. In-grain lattice gradients became weaker; color variations in the IPF maps and grain bending in the GROD maps became almost invisible. These observations suggest a strong GND

density reduction after irradiation at elevated (430°C) temperature in the EBR-II fast reactor, in contrast to the BOR-60 irradiation conditions.

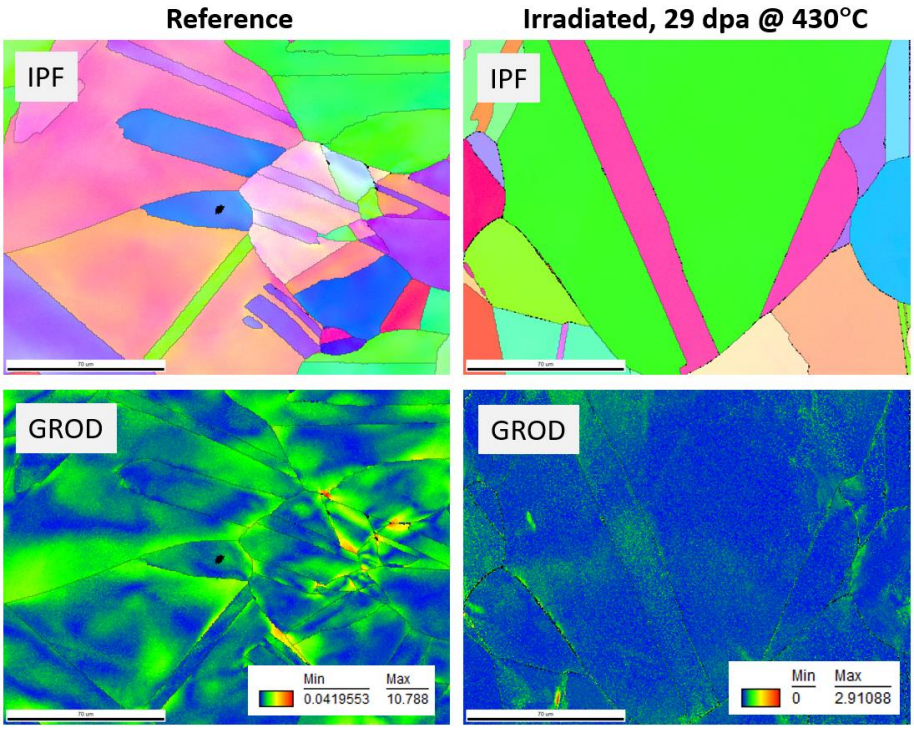

Figure 21. EBSD IPF and GROD maps for reference and EBR-II irradiated 304L steel (irradiation temperature: ~430°C).

Additional data analysis and, ideally, more data are needed; nevertheless, as a preliminary result, one may expect that "hot spots" generated by occasional deformation will exist for a long time under the LWR-relevant conditions (~320°C irradiation). In contrast, irradiation at 405° may lead to a strong reduction in GND density and "hot spots" or dislocation pileups, created by occasional deformation, may disappear.

5. SUMMARY AND CONCLUSIONS

This report documents experimental results on SEM-EBSD in situ mechanical tests performed with high-dose (up to 125 dpa) specimens of austenitic steels—materials of LWR-in-core components. Authentic archive materials were retrieved and included in the testing.

The collected datasets cover mechanical behavior, microstructure evolution, formation of the localized deformation areas, appearance and development of in-grain misorientation gradients, and microfracture events. Additionally, the report evaluates data collected in recent years and investigates the possible misorientation evolution under irradiation. The report introduces and briefly evaluates the concept of in-service-induced damage as an irradiation-assisted stress-corrosion cracking precursor.

Coupled with IASCC test results and data provided by electrochemical microscopy (both activities are being performed under the Light Water Reactor Sustainability (LWRS) Materials Reliability Program task), the outcome of the work presented here is important for understanding deformation mechanisms in materials irradiated to high-damage doses after long-term in-service life or for the case of reactor lifetime extension.

6. ACKNOWLEDGMENTS

This manuscript has been authored by UT-Battelle LLC under contract DE-AC05-00OR22725 with the US Department of Energy (DOE). The US government retains and the publisher, by accepting this manuscript for publication, acknowledges that the US government retains a nonexclusive, paid-up, irrevocable, worldwide license to publish or reproduce the published form of this manuscript or allow others to do so, for US government purposes.

The research was supported by the DOE Office of Nuclear Energy, for the LWRS program research and development effort. The authors would like to thank the CEA and EDF, and to personally thank Dr. B. Tanguy (CEA) for providing archive material (304L and 316L steels) for specimens irradiated in the BOR-60 fast reactor. Additionally, the authors would like to thank Dr. F. A. Garner (Radiation Effect Consulting) for providing archive 304L steel for the "Hex block" material irradiated in the EBR-II fast reactor. Authors would like to thank Dr. X. Chen (ORNL) for reviewing the report and providing valuable comments and suggestions, and L. Varma (ORNL) for help with document preparation.

REFERENCES

[1] K. Fukuya, H. Nishioka, K. Fujii, T. Miura, Y. Kitsunai, Local strain distribution near grain boundaries under tensile stresses in highly irradiated SUS316 stainless steel, J. Nucl. Mater. 432 (2013) 67–71.

[2] K. Fukuya, M. Nakano, K. Fujii, T. Torimaru, IASCC susceptibility and slow tensile properties of highly-irradiated 316 stainless steels, J. Nucl. Sci. Technol. 41 (2004) 673–681.

[3] Z. Jiao, G. Was, Impact of localized deformation on IASCC in austenitic stainless steels, J. Nucl. Mater. 408 (2011) 246–256.

[4] M. Kamaya, Assessment of local deformation using EBSD: Quantification of local damage at grain boundaries, Mater. Charact. 66 (2012) 56–67.

[5] C. Caer, R. Pesci, Local behavior of an AISI 304 stainless steel submitted to in situ biaxial loading in SEM, Mater. Sci. Eng. A. 690 (2017) 44–51.

[6] A. Järvenpää, M. Jaskari, J. Man, L.P. Karjalainen, Austenite stability in reversion-treated structures of a 301LN steel under tensile loading, Mater. Charact. 127 (2017) 12–26.

[7] M.N. Gussev, K.J. Leonard, In situ SEM-EBSD analysis of plastic deformation mechanisms in neutron-irradiated austenitic steel, J. Nucl. Mater. 517 (2019) 45–56.

[8] M.N. Gussev, G.M. de Bellefon, T.M. Rosseel, Analysis of Localized Deformation Processes in Highly Irradiated Austenitic Stainless Steel through In Situ Techniques, Oak Ridge National Lab.(ORNL), Oak Ridge, TN (United States), 2019.

[9] F. Garner, T. Okita, Y. Isobe, M. Sagisaki, J. Etoh, T. Matsunaga, P. Freyer, Y. Huang, J. Wiezorek, D. Porter, Measurement of void swelling in thick non-uniformly irradiated 304 stainless steel blocks using nondestructive ultrasonic techniques, Idaho National Laboratory (INL), 2001.

[10] V. Pastukhov, S. Averin, V. Panchenko, I. Portnykh, P. Freyer, L. Giannuzzi, F. Garner, Application of backscatter electrons for large area imaging of cavities produced by neutron irradiation, J. Nucl. Mater. 480 (2016) 289–300.

[11] Q. Yan, J. Gigax, D. Chen, F. Garner, L. Shao, Monte Carlo modeling of cavity imaging in pure iron using back-scatter electron scanning microscopy, J. Nucl. Mater. 480 (2016) 420–428.

[12] M.N. Gussev, S.R. Clark, J.T. Dixon, K.J. Leonard, Preparation and Analysis of Austenitic Stainless Steel Samples Irradiated at Very High Damage Doses, ORNLTM-2018113792. (2018).

[13] M. Gussev, N. Bibhanshu, E. Cakmak, J. Dixon, Analysis of Deformation Localization Mechanisms in Highly Irradiated Austenitic Stainless Steel via In Situ Techniques, (2020).

[14] A.J. Wilkinson, G. Meaden, D.J. Dingley, High-resolution elastic strain measurement from electron backscatter diffraction patterns: new levels of sensitivity, Ultramicroscopy. 106 (2006) 307–313.

[15] A. Wilkinson, E. Clarke, T. Britton, P. Littlewood, P. Karamched, High-resolution electron backscatter diffraction: an emerging tool for studying local deformation, J. Strain Anal. Eng. Des. 45 (2010) 365–376.

[16] H.J. Lee, C.H. Cho, M.W. Nam, H.J. Yoo, S.-Y. Hong, Eddy current testing of type-439 stainless steel tubing using magnetic saturation technique, J. Mech. Sci. Technol. 26 (2012) 2081–2085.

[17] S. Fujibayashi, T. Ohtsuka, T. Endo, Creep damage development of a 1.25 Cr-0.5 Mo steel weldment exposed to long term service, Tetsu--Hagané. 88 (2002) 326–333.